Iron-iron oxide supported palladium catalyst for the interconversion of formate and carbon dioxide

Wei-Jyun Wang, Frankie Roberts, Stena Peterson, Su Ha, Louis Scudiero, Romain Coustel, Martine Mallet, Mustapha Abdelmoula, Christian Ruby

Iron-Iron Oxide Supported Palladium Catalyst for the Interconversion of Formate and Carbon Dioxide

Wei-Jyun Wang[b], *Frankie Roberts*[c], *Stena Peterson*[c], *Su Ha*[b*], *Louis Scudiero*[a*]
Romain Coustel[d], *Martine Mallet*[d], *Mustapha Abdelmoula*[d], *Christian Ruby*[d]

[a] Chemistry Department and Materials Science and Engineering Program, Washington State University, Pullman, WA 99164, USA

[b] The Gene and Linda Voiland School of Chemical Engineering and Bioengineering, Washington State University, Pullman, WA 99164, USA

[c] Chemistry Department, Washington State University, Pullman, WA 99164, USA

[d] Université de Lorraine, CNRS, LCPME, F-54000 Nancy, France

*Corresponding Authors: Prof. Su Ha (suha@wsu.edu) and Prof. Louis Scudiero (scudiero@wsu.edu)

Abstract

Synthesized palladium-coated iron-iron oxide (Fe@FeO_x/Pd) nanoparticles (NPs) using the successive salt reduction method are tested for their activity and stability toward formate oxidation (FO) and electrochemical CO_2 reduction to formate (eCO_2RF). The experimental results for FO show a current density at 0.12V vs. $Ag/AgCl_2$ 16 times higher than for Pd that could be sustained at a value of 1.65 mA/cm^2 for more than 1h. Furthermore, the same catalyst displays a higher current density with a faradaic efficiency (FE) of 95.6 % toward the eCO_2RF, and exhibits a lower degree of CO adsorption. The iron-iron oxide interaction with the overlayer palladium is characterized by TEM/EDX, XPS/UPS, Mössbauer spectroscopy, and electrochemical techniques such as cyclic voltammetry (CV) and chronoamperometry (CA). NMR is used to estimate the amount of formate produced by the eCO_2RF. A positive binding energy shift of the Pd 3d peak and the upshift of the d-band center as measured by XPS compared to monometallic homemade Pd NPs confirm that the electronic perturbation of the catalyst surface plays a major role in enhancing the performance of Fe@FeO_x/Pd for both FO and eCO_2RF. Furthermore, the work function as measured by UPS for the Fe@FeO_x/Pd material is lower than that for monometallic Pd confirming a change in chemical properties of the catalyst surface. Finally, Mössbauer spectroscopy is used to determine the composition, structure and nature of all sites of the Fe@FeO_x substrate before use and the perturbation of their intrinsic properties by the Pd overlayer. This change in intrinsic properties of the Pd coated material provides additional explanations for the electrochemical improvement measured for this catalyst toward both FO and eCO_2RF.

Keywords: Iron/iron oxide-palladium, TEM, XPS, UPS, Mössbauer, CV, CA, NMR, formate oxidation and electrochemical CO_2 reduction.

1 Introduction

The increasing demand for more efficient portable electronic devices such as smartphones, digital cameras, iPads, and computers requires the development of more efficient small power sources. An efficient direct formate fuel cell (DFFC) could serve as such a power source [1-6]. Furthermore, a fuel cell combined with an electrochemical CO_2 reduction unit, which produces formate will allow the development of a quasi-regenerative small power source. As a fuel, formate is attractive because it is a liquid at room temperature, relatively inexpensive and can safely be stored. Moreover, it can be easily oxidized with a theoretical potential reaching 1.45 V, which is higher than the ones for methanol and ethanol fuel cells [7]. However, to make it a valuable alternative to other power sources, more efficient catalysts need to be developed. The commonly used catalysts for formate oxidation are precious metals such as platinum (Pt) and palladium (Pd). A Pd-based anode is extremely active for the electro-oxidation of formate and single cells using Pd as catalyst yield a reported maximum power density of 591 $mWcm^{-2}$ [8]. However, Pd is expensive, deactivates quite rapidly with operation time, and shows poor stability due to poisoning species like carboxyl and carbon monoxide. Efforts have been made to prepare bimetallic catalysts alloying Pd with other metals, such as Au and Cu as a way to enhance the activity toward formate oxidation (FO) [9-10]. In this work, the synthesis of a Pd-based catalyst involving Fe, which is one of the most abundant metals in the Earth's crust and is inexpensive, is used as supporting material for the development of a Pd-based bimetallic catalyst. $Fe@FeO_x/Pd$ catalyst shows high activity and stability toward both oxidation of formate and reduction of CO_2 and displays promise toward the interconversion between formate and carbon dioxide allowing the development of an improved sustainable and regenerative energy-storage system. The oxidation of formate by Fe@FeOx/Pd produces HCO_3^- at nearly neutral pH as a product that equilibrates with $CO_{2\,(aq)}$, which can then

be electrochemically reduced to formate. This latter conversion will contribute to the reduction of the amount of CO_2 released in the atmosphere, which is linked to climate change as demonstrated by Anderson's Earth System Models [11]. Therefore, Fe@FeO_x/Pd NPs could be used in both a DFFC and a CO_2 reduction unit to generate electricity without producing a net CO_2 emission, which would be very appealing technically and commercially as suggested by Vo et al. [12].

In this work, physical and chemical information on the synthesized materials are obtained by TEM and EDX. The electronic interaction between Fe@FeO_x and the overlayer Pd metal is measured by XPS/UPS. The latter techniques probe the binding energy of the Pd and Fe signals for the homemade Pd and the synthesized Fe@FeO_x, and for the Pd coated Fe@FeO_x, their d-band center positions, and their changes in work function. The activity and stability toward FO and eCO_2RF are measured by CV and CA, respectively. ^{57}Fe Mössbauer spectroscopy is carried out to provide supplemental information on the oxidation state, bonding property, and magnetic property of the Fe@FeO_x/Pd catalyst to support its electrochemical enhancement compared to that of the homemade Pd NP catalyst. Finally, nuclear magnetic resonance spectroscopy (NMR) is used to estimate the amount of formate produced from the electrochemical reduction of CO_2 for the synthesized Fe@FeO_x/Pd catalyst.

2 Experimental

2.1 Materials. Iron(II) sulfate heptahydrate ($FeSO_4.7H_2O$, 99%), palladium (II) chloride ($PdCl_2$, 99%), polyvinylpyrrolidone (PVP, the average molecular weight = 55000), sodium borohydride ($NaBH_4$), titanium (Ti) foil, and phenol (C_6H_5OH, 99%) were purchased from Sigma Aldrich. Hydrochloric acid (HCl, 36.5 %) was purchased from J.T. Baker. Deuterium oxide (D_2O, 99.9%) and sodium 2,2-dimethyl- 2-silapentane-5-sulfonatedss (DSS, 97%) were purchased from Cambridge Isotope Laboratories.

2.2 Preparation of the 0.5 M H_2PdCl_4. 443.5 mg of $PdCl_2$ was added into 5.0 mL of 1.6 M HCl solution. Then, the mixture was shaken at 80ºC until $PdCl_2$ was fully dissolved.

2.3 Synthesis of Iron@Iron Oxide Nanoparticles. A synthesis method for Fe@FeO_x NPs that was first proposed by Scott and co-workers was modified in this study as follows [27]: 8.0 mL of a 0.625 M $FeSO_4 \cdot 7H_2O$ aqueous solution was mixed in 10 mL of 2 M PVP methanol solution (in repeating unit). The light-yellow solution was stirred with a glass stir rod rigorously for 1 minute. 2.0 mL of a 1.82 M $NaBH_4$ aqueous solution was then added dropwise to the mixture, which resulted in the immediate reduction of the starting reagents into a thick black liquid. The solution was stirred for 3 minutes. 0.15 mL of 0.5 M H_2SO_4 was then added followed by the addition of 0.05 mL of 1 M glacial acetic acid to neutralize the remaining $NaBH_4$. Finally, the solution was centrifuged at 3400 rpm and then washed twice with methanol.

2.4 Coating of the Iron/Iron Oxide Nanoparticles. The Fe@FeOx NPs were dispersed into methanol and 133 μL of 0.5 M H_2PdCl_4 was added. The new solution was shaken for 30 seconds and then sonicated for 30 min to facilitate the galvanic displacement process. The solution was centrifuged at 3400 rpm and rinsed twice with methanol. The wet product was placed in a vacuum desiccator to dry.

2.5 TEM Characterization. The Fe@FeO_x and Fe@FeO_x/Pd NPs catalysts were imaged by TEM (FEI Technai G2 20 twin) and their particle sizes were analyzed by ImageJ software.

2.6 XPS and UPS Analyses. XPS spectra were obtained on a Kratos AXIS-165 using a monochromatized AlKα X-ray anode (1486.7 eV) and pass energy of 40 eV. The spectrometer was calibrated against the Ag $3d_{5/2}$ and Au $4f_{7/2}$ peaks at 368.3 and 84.0 eV, respectively. The samples were gently Ar^+ sputter at 4kV. UPS data were collected with a He lamp source which

produces a resonance line He I (21.21 eV) by cold cathode capillary discharge. A bias of -9.25 V was applied to the sample to shift the spectra out of the nonlinear region of the analyzer. The energy resolution was determined at the Fermi edge of a clean Cu foil to be better than 150 meV.

2.7 Mössbauer Measurements. Measurements were performed at different temperatures with a constant acceleration Mössbauer spectrometer, a 512 multichannel analyzer (Halder Electronic Gmbh), and a 50 mCi source of 57Co in Rh maintained at 25oC. Mössbauer spectra were collected in transmission mode. The 50 mCi source of 57Co in Rh matrix was maintained at room temperature and mounted at end of a Mössbauer velocity transducer. The spectrometer was calibrated with a 25 μm foil of α-Fe at 25oC. Analysis of the Mössbauer spectra consisted of the least-square fitting of data with a combination of a single line, two-peak quadrupole components (doublets) and, when present, six-peak magnetic hyperfine components (sextets). To fit the experimental data that give rise to the broadened spectra induced by the structural disorder, the Voigt-based fitting method of Rancourt and Ping [15] for quadrupole splitting distribution (QSDs) and magnetic hyperfine fields (HFDs) was used.

2.8 Electrochemical Characterization. Electrochemical measurements were performed using a BASi EC EpsilonTM potentiostat and a standard three-electrode cell. For our three-electrode cell, Pt mesh was used as a counter electrode, Ag/AgCl (3.5 M KCl) electrode as the reference electrode, and a rotating glassy carbon with our synthesized catalysts was used as the working electrode. The electrochemical formate oxidation measurements were performed in 0.5 M $KHCO_3$ + 0.25 M HCOOK electrolyte solution via cyclic voltammetry (CV) experiments at a scan rate of 20 mV/s. The eCO_2R measurements were also performed in 0.5 M $KHCO_3$ after bubbling CO_2 gas into the electrolyte for 30 mins via CV tests at a scan rate of 20 mV/s. The

electrochemical active surface area (ECSA) was determined using the Pd-oxide stripping peak and used to normalize the current densities [13-14].

$$\text{ECSA } (\text{cm}^2) = \frac{Q}{424\ \mu C/cm^2} \qquad (1)$$

where Q is the charge obtained by intergrading the area of the Pd-oxide reduction peak obtained by CV scans performed in 0.5 M H_2SO_4. Ti foil was coated with Fe@FeO_x/Pd NPs to make the working electrodes for the 4 and 20 hours long CA experiments of eCO_2RF. NMR was then used to estimate the amount of formate produced during the long-term CA measurements. The measurement details and data (Figure S1) are given in the Supporting Information.

3 Result and Discussion

3.1 TEM images and Chemical mapping. Figure 1 shows TEM images of the synthesized Fe@FeO_x NPs and the Pd coated Fe@FeO_x/Pd material. The average particle size for the core-shell Fe@FeO_x structure is about 9.5 ± 2.0 nm as determined by ImageJ software as shown in Figure 1a. The dark center region is pure Fe and the lighter color is FeO_x shell with a thickness of about 2.0 nm as shown in the insert. The TEM image of the Pd coated Fe@FeO_x material is displayed in Figure 1b. The image shows that the Fe@FeO_x particles are covered by a thin layer of Pd. The Pd coated Fe@FeO_x NPs size is about 11.7 ± 1.7 nm. The size difference between the Fe@FeO_x and Pd coated Fe@FeO_x suggests that the Pd thickness is relatively thin.

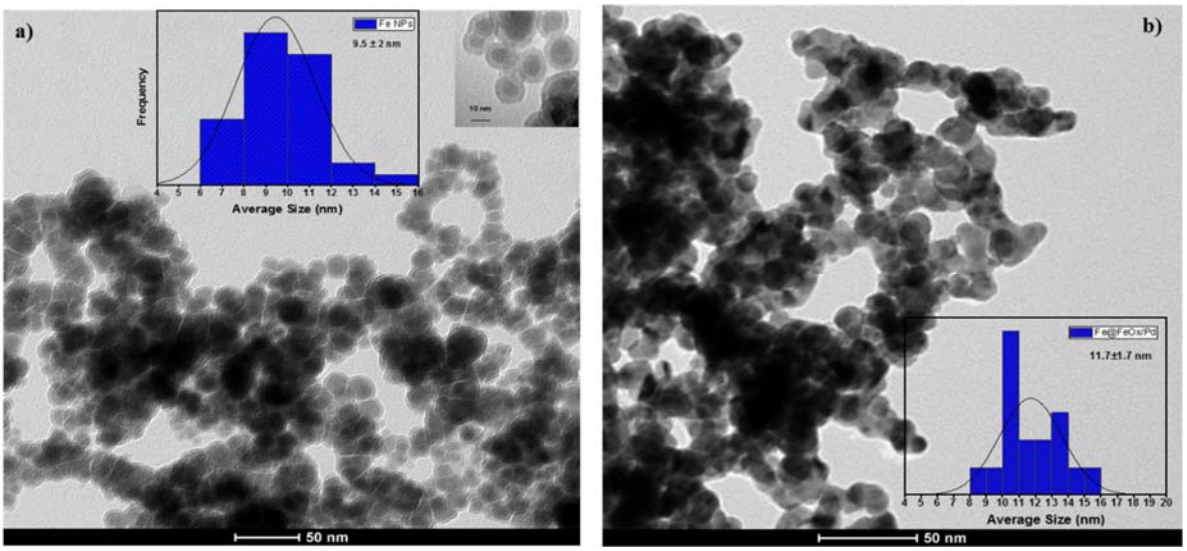

Figure 1. (a)TEM images of Fe@FeO_x NPs with an average size of about 9.5 nm and insert detailing the core-shell structure of Fe@FeO_x and its oxide layer, and (b) TEM images of Fe@FeO_x/Pd NPs with a size of about 11.7 nm.

Additional bright field HRTEM images and their associated chemical mappings of Fe-$L_{2,3}$, O-K and Pd-$M_{4,5}$ are shown in Fig.2. The elemental mappings in Fig. 2a confirm the core-shell structure of the synthesized Fe@FeO_x nanoparticles. Fig. 2b displays the chemical mapping of Fe and Pd and emphasizes the mode of growth of Pd showing full coverage of the Fe@FeO_x support.

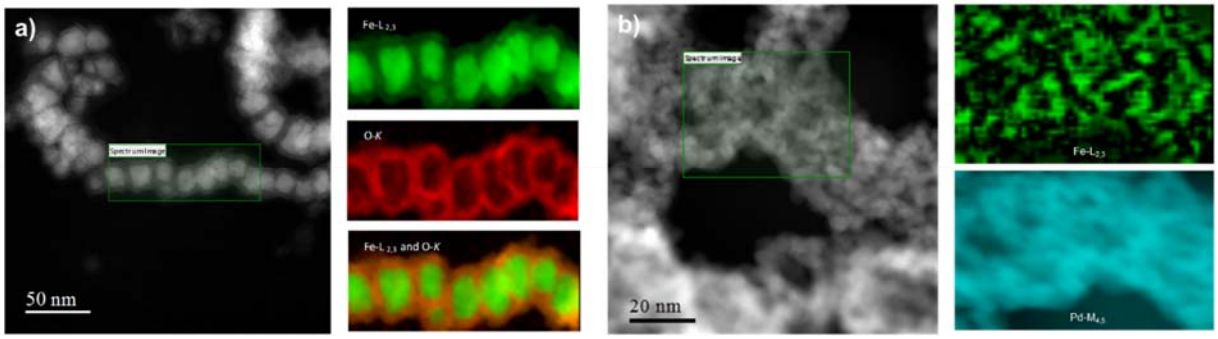

Figure 2. HRTEM images and their associated chemical mappings showing a) the core-shell structure of the Fe@FeO_x NPs and b) the distribution of Pd (blue) covering the Fe@FeO_x NPs (green).

3.2 XPS and UPS Analyses. XPS spectra of both Pd $3d_{5/2}$ and Fe 2p core levels for Fe@FeO_x NPs, Fe@FeO_x/Pd, and homemade Pd NPs are shown in Figure 3. The Fe 2p spectrum for Fe@FeO_x displays peaks attributed to metallic Fe^0 ($2p_{3/2}$ at ~707 eV) and FeO_x. Furthermore, the deconvolution of the oxide peak indicates the presence of Fe^{2+} (peak at BE ~710 eV), Fe^{3+} (peak at BE ~712 eV), and some mixture of Fe^{2+} / Fe^{3+} (peak at BE ~715 eV). The assignment of a weak peak at BE = 720 eV is ambiguous since both the Fe^0 $2p_{1/2}$ and the Fe^{3+} satellite are at that same energy. The spectrum for Fe@FeO_x/Pd shows a quasi-absent peak at 720 eV, a reduction of the amount of Fe^0 and Fe^{2+}, and a slight increase in Fe^{3+} species as indicated by the change in relative atomic percent concentration (At%). Although no BE shift is observed for Fe^0 a small negative shift is measured for both Fe^{2+} and Fe^{3+}.

The Pd $3d_{5/2}$ spectra for both the Fe@FeO_x/Pd material and homemade Pd NPs are shown in Figure 3b. A small positive BE shift is measured between the Fe@FeO_x/Pd material and the homemade Pd NPs. This energy shift suggests that electrons transferred from the Pd to the FeO_x modifying the electronic property of the Pd surface. This energy shift corolates with the negative shift measured for Fe^{2+} and Fe^{3+} species. The closest related study is the one by Spiridis et al. of Au deposited onto a 20-40 nm Fe_3O_4(001) film revealing a charge transfer from the Au clusters to the support (positive shift of the Au $4f_{7/2}$) leaving positively charged Au clusters, which was also confirmed by their Mössbauer analysis [15].

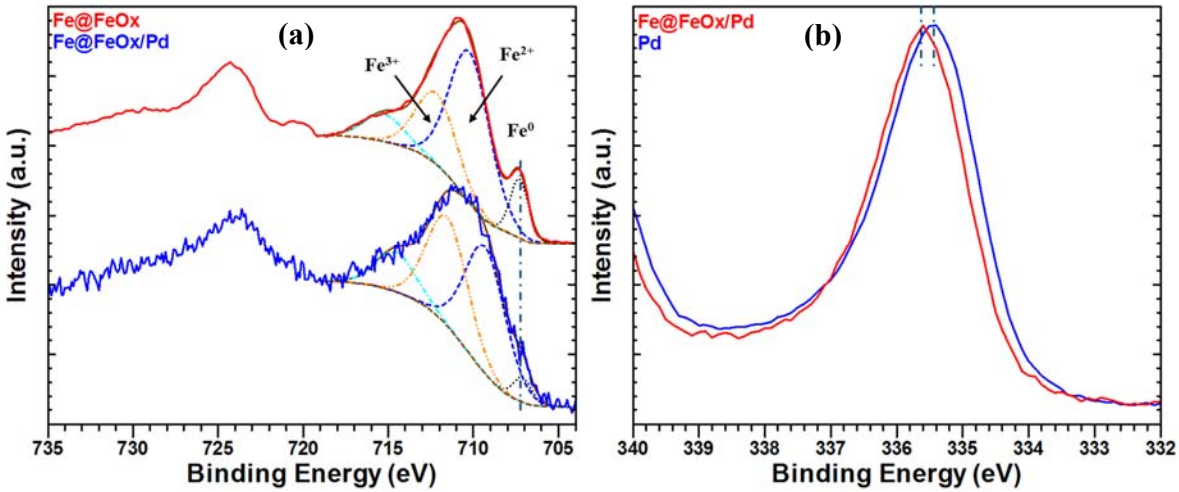

Figure 3. XPS spectra of **(a)** Fe 2p for Fe@FeO_x and Fe@FeO_x/Pd NPs and **(b)** Pd 3d for homemade Pd and Fe@FeO_x/Pd NPs.

The XPS valence band (VB) shown in Figure 4 is used to determine the d-band centers for all three samples given by the normalized first moment:

$$\mu_1 \equiv \frac{\int_{E_F}^{E} N(E)E\,dE}{\int_{E_F}^{E} N(E)\,dE} \qquad (2)$$

The different features seen in the VB spectrum of Fe@FeO_x NPs are mostly attributed to Fe^{2+} and Fe^{3+} components as described by Fujii et al. in their XPS study and cluster-model calculation of iron oxide films grown by NO_2 assisted molecular bean epitaxy (MBE) [17]. The VB spectrum is also in relatively good agreement with the data obtained by Schedel-Niedrig et al. for an ultrathin film of iron oxide deposited onto Pt (111), and those measured and calculated by Sherwood et al. for Fe and its oxides [18-19]. The VB for both the Pd monometallic and the Fe@FeO_x/Pd catalyst are also shown in Figure 4. The d-band center shifts from 2.45 eV for Pd to 2.59 eV for the Fe@FeO_x/Pd. This energy shift away from the Fermi level confirms charge transfer from Pd to FeO_x, in agreement with the shift observed for Pd $3d_{5/2}$ core level and the Fe species due to the

combination of both the strain and the electronic (or ligand) effects. As the d-band center shifts away from the Fermi level, the adsorption strength of intermediates on the surface of the catalyst is expected to weaken [20], which leads to the modification of the overall reaction rate [21].

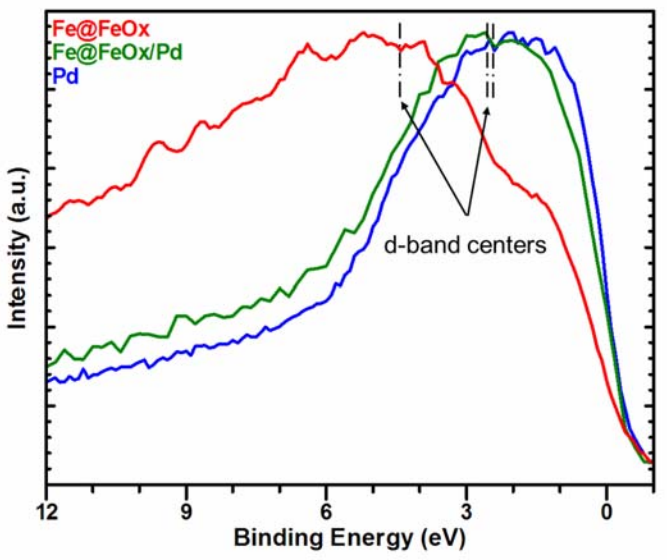

Figure 4. XPS valence band spectra for Fe@FeO_x, Fe@FeO_x/Pd, and homemade Pd NPs.

Figure 5 exhibits the HeI secondary electron cutoff for Fe@FeO_x, Fe@FeO_x/Pd, and Pd. A change of -0.40 eV in the work function for the Fe@FeO_x/Pd catalyst compared to the homemade monometallic Pd is measured. This change is important due to the sensitivity of the work function to any chemical change of a surface property; its measurement can give valuable insight into the condition of the Pd surface. Theoretical studies by Schleifer et al., Pacchioni et al., Jiang et al. and Kiejna et al. demonstrate a relationship between work function and surface chemical structures [22 – 25]. The change in work function is mainly due to an electrostatic effect, a charge transfer, and a lattice mismatch effect. Kiejna et al. calculated the change in work function for Pd covered Fe_3O_4 (111) by DFT and DFT+U to be -0.67 eV, which is in relatively good agreement with our

experimental result [25]. Although studies of dielectric films and highly ionic materials deposited on metals have been theoretically investigated, experimental studies on the work function change induced by a deposited metal on a different metal or metal oxide are unfortunately quasi-inexistent. More important, the theoretical study by Jiang et al. of Pd-based bimetallic surfaces demonstrates that there is a correlation between the following three parameters: d-band center, surface electron flow out, and work function [24].

In the present study, the decrease in the work function of Fe@FeO_x/Pd correlates with the increase of the d-band center, which suggests a charge transfer from the Pd overlayer to the Fe oxide in agreement with our XPS Pd 3d and VB measurements. The electron deficiency at the surface of Fe@FeO_x/Pd material could result in a significant change in its electrocatalytic performances (i.e., both FO and eCO_2RF) compared to that of monometallic Pd.

To investigate further the effect of coating Fe@FeO_x NPs with Pd, Mössbauer spectra of Fe@FeO_x and Fe@FeO_x/Pd obtained at room temperature are compared.

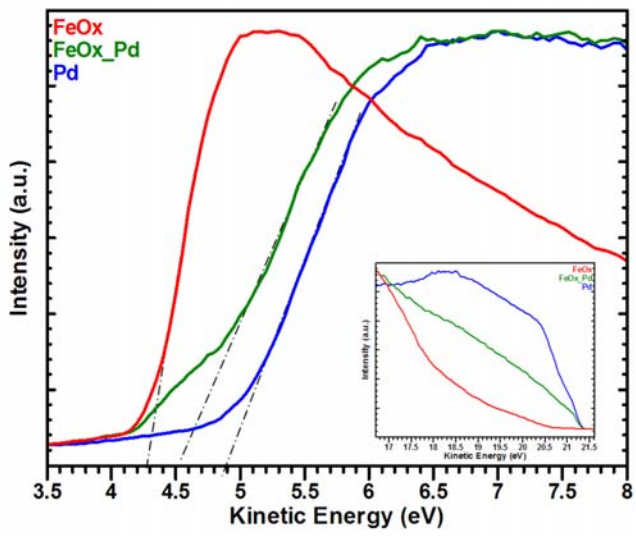

Figure 5. HeI spectra of secondary electron cutoffs for Fe@FeO_x, Fe@FeO_x/Pd and Pd NPs, the inset displays the Fermi energy region for all three NPs.

3.3 Mössbauer Measurements. Mössbauer spectroscopy probes changes in the energy levels of an atomic nucleus in response to its environment [26]. Mössbauer spectra of both the Fe@FeO_x NPs and the Fe@FeO_x/Pd catalyst were acquired at temperatures ranging from 298K to 4K. Figure 6 focuses on the spectra measured at 298 K. The interaction between Pd and its support is discussed to understand further the activity improvement measured for the Fe@FeO_x/Pd material toward both the electrochemical formate oxidation and CO_2 reduction.

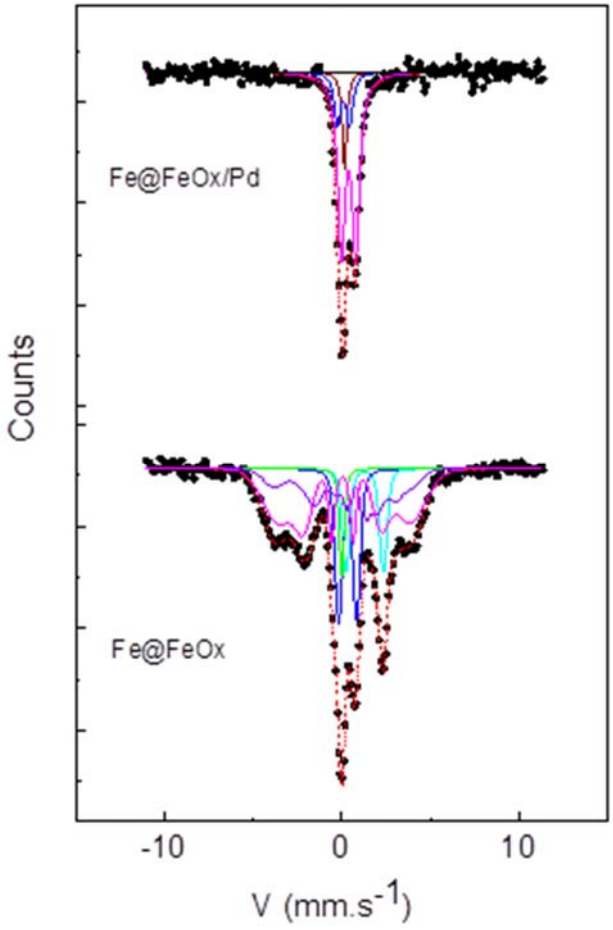

Figure 6. Mössbauer spectra for the Fe@FeO_x and Fe@FeO_x/Pd NPs obtained at room temperature.

The room temperature spectrum for Fe@FeO_x NPs displays three doublets (D1 for Fe^{2+}, D2 and D3 for Fe^0) and two sextets (S1 and S2) components. The paramagnetic component is described as the superimposition of elemental subspectra D2 and D3 whose low-value hyperfine parameters (CS and Δ) differ respectively from those of the doublet D1. The larger values of CS and Δ for D1 are attributed to the Fe^{2+} state whereas the small one to Fe^0 state. The magnetic component constituted of two sextets is typically due to the superparamagnetic behavior of the material.

The spectrum of the Pd coated Fe@FeO_x NPs shows a significant change in the lineshape. It can be easily fitted with one singlet and two quadrupole doublets (magnetite and Fe^0). We can observe the disappearance of the doublet corresponding to the Fe^{2+} site when the spectrum of Fe@FeO_x/Pd NPs is compared to the spectrum of Fe@FeO_x NPs. Another effect due to the presence of Pd on the Mössbauer spectrum measured at 298 K is the absence of relaxation phenomenon observed for Fe@FeO_x NPs with the presence of broad sextets typical of the superparamagnetic effect. Therefore, coating Fe@FeO_x NPs with a Pd overlayer appears to modify the magnetic properties of the Fe@FeO_x substrate at 298 K through charge transfer, changing the overall oxidation state of Fe, particle sizes, and system from superparamagnetic state (Fe@FeO_x) to paramagnetic state (Fe@FeO_x/Pd).

Since the nuclear hyperfine structure in isotope probe (^{57}Fe) that is measured results from the perturbation to the nuclear levels of the Mössbauer transition, Mössbauer spectroscopy is a sensitive probe of local electronic structure and by extension, of the local crystallographic, magnetic, and chemical environments. The disappearance of Fe^{2+} site could be explained by its oxidation coupled with the reduction of Pd^{2+} to Pd^0 during Pd film formation as observed by XANES in agreement with Yao et al. [27]. The absence of superparamagnetism at room

temperature for the Fe@FeO_x/Pd catalyst could be due to a chemical interaction between Pd and Fe species as already observed with XPS.

3.4 CV and CA measurements. Figure 7 shows CV results for homemade Pd and for Fe@FeO_x/Pd in 0.5 M $KHCO_3$ and 0.25 M HCOOK solution at a scan rate of 20 mV s^{-1} under N_2 flow obtained at room temperature (a) and CA data of the same catalysts in the same electrolyte (b) for investigating their performances toward the FO. According to Figure 7a, the current density measured at potential 0.12 V vs. Ag/AgCl is 16 times higher for Fe@FeO_x/Pd than for homemade Pd. CA measurements conducted at the same potential also show improved stability of the bimetallic catalyst, sustaining higher current density than the monometallic Pd for more than 3600 s as seen in Figure 7b. These measurements reveal the electrochemical superiority of the Fe@FeO_x/Pd NPs toward the oxidation of formate compared to that of homemade Pd NPs.

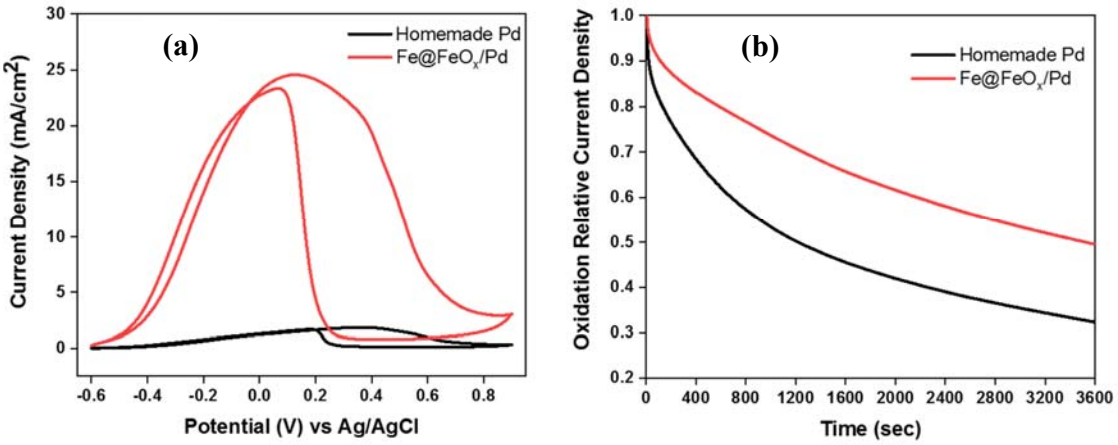

Figure 7. (a) Room-temperature CV results for Fe@FeO_x/Pd and Pd NPs in 0.5 M $KHCO_3$ + 0.25M HCOOK at a scan rate of 20 mV/s under N_2 atmosphere, and **(b)** CA measurements at a fixed potential of 0.12 V of the same nanoparticles in the same electrolyte.

Figure 8 displays CV data for both catalysts (i.e., Fe@FeO_x/Pd and Pd) in CO_2 saturated (pH = 7.2) 0.5 M $KHCO_3$ electrolyte for investigating their electrochemical reduction performance. A significant increase in current density at a potential of -0.75 V vs. Ag/AgCl is measured for the Fe@FeO_x/Pd catalyst compared to that of the homemade Pd catalyst (1.65 mA/cm^2 vs. 0.02 mA/cm^2). At the potential of -0.75 V, the product of the eCO_2R is expected to be mostly formate with a minimum production of CO. The insert in Figure 8 exhibits the CV data obtained for the Fe@FeO_x catalyst under similar conditions. A negligible current is measured in the potential region where formate is produced. To determine the faradaic efficiency (FE%) of Fe@FeO_x/Pd and homemade Pd toward eCO_2RF, CA measurements were conducted for 4 hours at -0.75 V vs. Ag/AgCl in CO_2 saturated 0.5 M $KHCO_3$. Based on their corresponding ^{1}H-NMR data (shown in SI Fig. S1), the FE% values were determined to be 95.6% and 91.6% for Fe@FeO_x/Pd and homemade Pd, respectively. This result is in very good agreement with the value of 97% obtained by Klinkova et al. on Pd at -0.82 V vs. Ag/AgCl [28]. However, the activity of our Fe@FeO_x/Pd toward CO_2 reduction into formate is much higher than their best Pd sample (Pd NPs enclosed by high-index facets). Under similar conditions, the starting current density of the Fe@FeO_x/Pd sample used in this study at -0.75 V vs. Ag/AgCl is about 56 times higher than the current density measured at -0.82 V vs. Ag/AgCl by Klinkova et al. These CV and CA results for Fe@FeO_x/Pd and the high FE value indicate that the modification of the surface electronic property of Pd surface by the presence of Fe@FeO_x significantly improves its eCO_2R activity toward formate production.

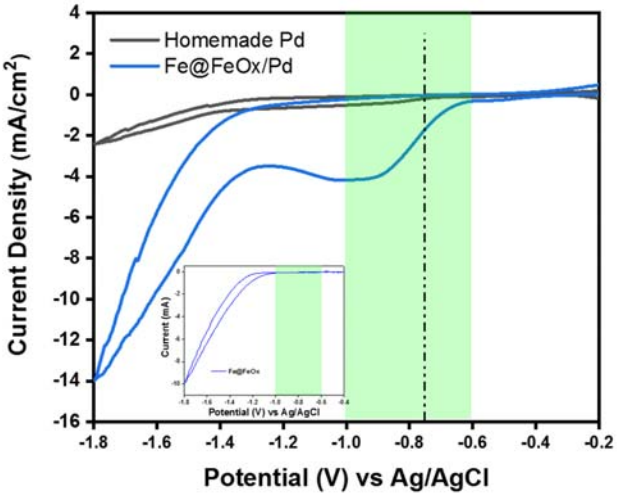

Figure 8. Cyclic voltammograms for homemade Pd and for Fe@FeO_x/Pd NPs in CO_2 saturated 0.50 M $KHCO_3$. The green region represents the range of potential for producing formate via CO_2 reduction. The insert displays a CV data for Fe@FeO_x NPs measured in the same electrolyte.

Finally, Figure 9 displays data for generating formate from CO_2 via eCO_2R and oxidizing this CO_2-derived formate to produce electricity. This process simulates the regenerative fuel cell concept. Figure 8a shows the CA experiment of Fe@FeO_x/Pd conducted for 32 hours in CO_2 saturated 0.5 M $KHCO_3$. Because the potentiostat used is unable to record continuously CA data for more than 4 hours, the 32-hour measurement had to be restarted manually producing current gaps. Similarly, the electrolyte had to be replenished generating spikes denoted with stars. During the first 28 hours, the Fe@FeO_x/Pd working electrode was operated under the eCO_2R operation mode by applying -0.75 V vs. Ag/AgCl for reducing CO_2 into formate. In order to verify that formate was produced via eCO_2R, the CA experiment was stopped briefly at 20 and 24 h to perform CV scans (shown in Figure 9b). At t = 28 h, the cell operation mode was switched to operate for 4 hours under the formate oxidation mode (i.e., direct formate fuel cell operation mode) by applying -0.067 V vs. Ag/AgCl for oxidizing the CO_2-derived formate (shown in Figure 9a). These

measurements demonstrate that Fe@FeO_x/Pd is a promising bifunctional electro-catalyst for the development of a sustainable energy system capable of storing intermittent renewable electrical energy into chemical energy by converting CO_2 into formate and oxidize this CO_2-derived formate to produce electricity.

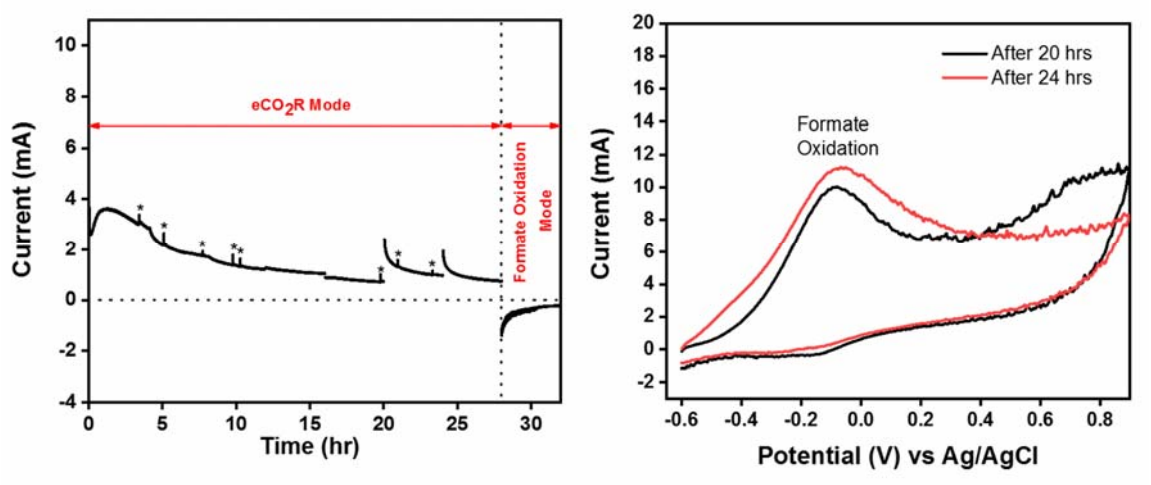

Figure 9. (a) 32 hours CA conducted in CO_2 saturated 0.5 M $KHCO_3$ at a potential of -0.75 V vs. Ag/AgCl. At t = 28 hours, a potential of -0.067 V vs. Ag/AgCl was applied to oxidize the CO_2-derived formate (Note that the current spikes are caused by the replenishment of the electrolyte and current gaps by the restart of the CA). **(b)** CV scans were performed at t = 20 and 24 hours during the CA measurement.

4 Conclusion

The Pd coated core-shell Fe@FeO_x catalyst prepared via the successive salt reduction method display a high catalytic activity and stability toward the interconversion of formate and CO_2. The analytical techniques utilized to investigate this bimetallic nano-catalyst demonstrate that the Pd surface electronic properties are modified by the underlying Fe@FeO_x substrate resulting in higher activity and stability for the Fe@FeO_x/Pd toward both the electrochemical CO_2 reduction to formate and oxidation of formate. We demonstrated that this bimetallic catalyst exhibits a two

orders of magnitude increase in current density at -0.75V and a 95.6 % FE toward formate production from the electrochemical reduction of CO_2. In addition, it displays a 16 times higher current density than that for the homemade Pd catalyst toward the formate oxidation. Therefore, this bimetallic catalyst shows promise for the development of sustainable and regenerative fuel cells, which will combine a direct formate fuel cell and a CO_2 reduction unit into a single regenerative energy system.

Acknowledgments

We would like to thank the Murdock Charitable Trust for its financial support in upgrading our existing XPS instrument and the continuous support of Washington State University. The Mössbauer spectroscopy part in this work was supported by means of the Spectroscopy and Microscopy Core Facility of SMI LCPME (Universite de Lorraine, CNRS, LCPME-https://www.lcpme.ul.cnrs.fr), which is gratefully acknowledged.

References

1. E.H. Yu, X. Wang, U. Krewer, L. Lid, K. Scott, Direct oxidation alkaline fuel cells: from materials to systems, Energy Environ. Sci 5 (2012) 5668-5680. https://doi.org/10.1039/C2EE02552C
2. L. An, T.S. Zhao, J.B. Xu, A bi-functional cathode structure for alkaline-acid direct ethanol fuel cells, Int. J. Hydrogen Energy 36 (2011) 13089-13095. https://doi.org/10.1016/j.ijhydene.2011.07.025
3. E. Antolini, E.R. Gonzalez, Alkaline direct alcohol fuel cells, J. Power Sources 195 (2010) 3431-3450. https://doi.org/10.1016/j.jpowsour.2009.11.145

4. L. An, T.S. Zhao, S.Y. Shen, Q.X. Wu, R. Chen, An alkaline direct oxidation fuel cell with non-platinum catalysts capable of converting glucose to electricity at high power output, J. Power Sources 196 (2011) 186-190. https://doi.org/10.1016/j.jpowsour.2010.05.069

5. L. An, L. Zeng, T.S. Zhao, An alkaline direct ethylene glycol fuel cell with an alkali-doped polybenzimidazole membrane, Int. J. Hydrogen Energy 38 (2013) 10602-10606. https://doi.org/10.1016/j.ijhydene.2013.06.042

6. Y.S. Li, Y.L. He, Layer reduction method for fabricating Pd-coated Ni foams as high-performance ethanol electrode for anion-exchange membrane fuel cells, RSC Adv. 4 (2014) 16879-16884. https://doi.org/10.1039/C4RA01399A

7. Y.S. Li, Y.L. He, Performance characteristics of air-breathing anion-exchange membrane direct ethanol fuel cells, Int. J. Hydrogen Energy 37 (2012) 15334-15338. https://doi.org/10.1016/j.ijhydene.2013.07.042

8. L. An, R. Chen, Direct formate fuel cells: A review, J. Power Sources 320 (2016), 127-139. https://doi.org/10.1016/j.jpowsour.2016.04.082

9. J. Noborikawa, J. Lau, J. Ta, S. Hu, L. Scudiero, S. Derakhsha, S. Ha, J.L. Haan, Palladium-copper electrocatalyst for promotion of oxidation of formate and ethanol in alkaline media, Electrochimica Acta 137 (2014) 654-660. https://doi.org/10.1016/j.electacta.2014.04.188

10. S.G. da Silva, J.C.M. Silva, G.S. Buzzo, E.V. Spinac_e, A.O. Neto, Mônica H. M. T. Assumpção, PdAu/C electrocatalysts as anodes for direct formate fuel cell, Electrocatalysis 6 (2015) 442-446. https://doi.org/10.1007/s12678-015-0262-1

11. T.R. Anderson, Ed. Hawkins, P.D. Jones, CO_2, the greenhouse effect and global warming: from the pioneering work of Arrhenius and Callendar to today's Earth System Models, Endeavour 40 (2016) 178-187. https://doi.org/10.1016/j.endeavour.2016.07.002

12. T. Vo, K. Purohit, C. Nguyen, B. Biggs, S. Mayoral, J.L. Haan, Formate: an energy storage and transport bridge between carbon dioxide and a formate fuel cell in a single device ChemSusChem 8 (2015) 3853-3858. https://doi.org/10.1002/cssc.201500958

13. P.N. Bartlett, B. Gollas, S. Guerion, J. Marwan, The preparation and characterisation of H_1-e palladium films with a regular hexagonal nanostructure formed by electrochemical deposition from lyotropic liquid crystalline phases Phys. Chem. Chem. Phys. 4 (2002) 3835-3842. https://doi.org/10.1039/B201845D

14. D.A.J. Rand, R. Woods, A study of the dissolution of platinum, palladium, rhodium and gold electrodes in 1 M sulphuric acid by cyclic voltammetry. J. Electroanal. Chem. Int. Electrochem. **35**, 1972, 209-218. https://doi.org/10.1016/S0022-0728(72)80308-5

15. N. Spiridis, R.P. Socha, B. Handke, J. Haber, M. Szczepanik, J. Korecki, Cluster–support interaction in Au–Fe_3O_4 system. Catalysis Today 169 (2011), 24-28. https://doi.org/10.1016/j.cattod.2010.08.027

16. D.G. Rancourt, J.Y. Ping, Voight-based methods for arbitrary-shape static hyperfine parameter distributions in Mossbauer spectroscopy. Nucl. Instrum. Methods Phys. Res., B 58 (1991) 85-97. https://doi.org/10.1016/0168-583X(91)95681-3

17. C. Gabrielli, P. P. Grand, A. Lasia , H. Perrota, Investigation of hydrogen adsorption and absorption in palladium thin films : II. cyclic voltammetry. J. Electrochem. Soc. 151 (2004) A1937-A1942. https://doi.org/10.1149/1.1797035.

18. W. Temesgen, P.M.A. Sherwood, Analytical utility of valence band X-ray photoelectron spectroscopy of iron and its oxides, with spectral interpretation by cluster and band structure calculations. Anal. Bioanal. Chem. 373 (2002) 601-608. https://doi.org/10.1007/s00216-002-1362-3

19. Th. Schedel-Niedrig, W. Weiss, R. Schlogl, Electronic structure of ultrathin ordered iron oxide films grown onto Pt(111). Phys. Rev. B, 52 (1995) 17449-17460. https://doi.org/10.1103/PhysRevB.52.17449

20. S. Hu, F. Che, B. Khorasani, M. Jeon, C.W. Yoon, JS. McEwen, L. Scudiero, S. Ha, Improving the Electrochemical Oxidation of Formic Acid by Tuning the Electronic Properties of Core@Shell Pd-based Nanoparticles, Applied Catalysis B: Environmental, 254 (2019) 685-692. https://doi.org/10.1016/j.electacta.2020.137023

21. Bligaard, T. and J.K. Nørskov, Ligand effects in heterogeneous catalysis and electrochemistry. Electrochimica Acta 52 (2007) 5512-5516. https://doi.org/10.1016/j.electacta.2007.02.041

22. T.J. Fabish, D.E. Schleifer, Surface chemistry and carbon black work function. Carbon. 22 (1984) 19-38. https://doi.org/10.1016/0008-6223(84)90129-5

23. S. Prada, U. Martinez, G. Pacchioni, Work function changes induced by deposition of ultrathin dielectric films on metals: theoretical analysis. Phys. Rev. B. 78 (2008) 235423. https://doi.org/10.1103/PhysRevB.78.235423

24. ZB Ding, F. Wu, YC Wang, and H. Jiang, Theoretical studies of the work functions of Pd-based bimetallic surface. J. Chem. Phys. 142 (2015) 214706. https://doi.org/10.1063/1.4921895

25. A. Kiejna, T. Ossowski, T. Pabisiak, Surface properties of the clean and Au/Pd covered Fe_3O_4(111): DFT and DFT+U study. Phys. Rev. B. 85 (2012) 125414. https://doi.org/10.1103/PhysRevB.85.125414

26. P. Gütlich, Fifty Years of Mössbauer Spectroscopy in Solid State Research –Remarkable Achievements, Future Perspectives. J. Inorg. Gen. Chem. 638 (2012) 15-43. https://doi.org/10.1002/zaac.201100416

27. Y. Yao, C. Patzig, Y. Hu, R. W. J. Scott, In Situ X-ray Absorption Spectroscopic Study of Fe@Fe_xO_y/Pd and Fe@FexOy/Cu Nanoparticle Catalysts Prepared by Galvanic Exchange Reactions. J. Phys. Chem. C 119 (2015) 21209−21218. https://doi.org/10.1021/acs.jpcc.5b06155.

28. A. Klinkova, Phil De Luna, Cao-Thang Dinh, O. Voznyy, E.M. Larin, E. Kumacheva, E.H. Sargent, Rational Design of efficient palladium catalyst for electroreduction of carbon dioxide to formate, ACS Catalysis, 6 (2016) 8115-8120. https://pubs.acs.org/doi/abs/10.1021/acscatal.6b01719.